PAPER

Check for updates

Printing of tin perovskite solar cells *via* controlled crystallization†

Xuan Li,‡[ae] Giuseppe Nasti, [ID] ‡[bc] Chris Dreessen,[d] Janardan Dagar,[e] Rico Meitzner,[e] Davide Amoroso,[c] Pier Luca Maffettone,[c] Thomas Kirchartz, [ID] [df] Eva Unger, [ID] [e] Antonio Abate*[ce] and Stoichko D. Dimitrov [ID] *[a]

The urgent need for sustainable electricity has driven progress in solar technologies, with perovskite photovoltaics standing out as a top contender. However, the presence of toxic lead in current perovskite devices necessitates the exploration of alternative materials. This study addresses the challenges associated with tin perovskite fabrication and the industrial scale-up of this lead-free technology. It introduces a new approach to regulate the key process of crystallization, involving a combination of new additives and a gas pulse to trigger and subsequently control nucleation and crystal growth. *In situ* optical spectroscopy probed the crystallization and enabled the optimization of the printing conditions. Solar cells were fabricated with a power conversion efficiency of 5.38% for 0.1 cm^2, 4.02% for 1 cm^2 and 2.31% for 5 cm^2 devices. They were tested under indoor lighting conditions and functioned at similar efficiency levels, thereby demonstrating the potential of this technology for commercial applications. Our new crystallization control method for printing Sn perovskites enabled the fabrication of the first Sn-based solar cell *via* slot-die coating, which is ideally suited for roll-to-roll manufacturing. This innovation opens new avenues for the development of fully printed lead-free perovskite photovoltaics, contributing significantly to the advancement of sustainable energy technologies.

Introduction

Metal-halide organic–inorganic perovskite solar cells have become the most popular emerging solar cell technology because of their potential to expand the number of applications for solar cells, enabling simpler manufacturing and increasing the efficiency of silicon devices. However, there are bottlenecks for their commercialization due to environmental concerns and health issues related to the presence of soluble Pb in the structure.[1] Sn is considered the most promising substitute for Pb in the perovskite crystal structure, as it offers similar electronic properties but potentially a lower toxicity and a smaller environmental impact.[2] Furthermore, Sn perovskites and

specifically the popular formamidinium Sn iodide (FASI) have a smaller bandgap (1.3 eV) and can reach 33% power conversion efficiency (PCE), which is higher than Pb-perovskite (31%) according to the Shockley–Queisser limit.[3] The highest efficiency achieved thus far for Sn-based perovskite solar cells is 16.05%,[4] compared to 26.7% for single-band gap Pb-based perovskite devices and 34.6%[5,6] for Pb perovskite/silicon tandem monolithic devices.

Sn-perovskite films have mostly been deposited *via* spin coating, which is a solution deposition technique used in conjunction with an antisolvent treatment and a heating step to fully convert the wet thin film into a perovskite semiconductor. A key feature of the fabrication process is that Sn perovskite crystallization is ultrafast, which is due to the greater Lewis acidity of Sn^{2+} compared to Pb^{2+}, leading to uncontrollable film nonuniformities.[7] Slowing down crystallization has been key to achieving a broader processing window and better-quality films.[7–9] One way to make this possible has been solvent engineering.[9–11] For example, Nasti *et al.* reported 4-(*tert*-butyl) pyridine (*t*BP) as a host solvent replacing the oxidative dimethyl sulfoxide (DMSO) to form a stable intermediate state that retards crystallization.[12] Another popular approach is based on using additives as regulators of the crystallization dynamics, such as Sn halides.[9] Both, SnCl$_2$ (ref. 13) and SnF$_2$ (ref. 14–16) form a Sn-rich environment that compensates for Sn vacancy defects and minimizes the oxidation of Sn^{2+}, thus achieving

[a]Department of Chemistry, School of Physical and Chemical Sciences, Queen Mary University of London, London, E1 4NS, UK. E-mail: s.dimitrov@qmul.ac.uk

[b]ENEA Research Center Portici, Piazzale Enrico Fermi 1, Portici, 80055, Italy

[c]Department of Chemical, Materials and Production Engineering, University of Naples Federico II, Piazzale Tecchio 80, Fuorigrotta, Naples, 80125, Italy. E-mail: antonio. abate@helmholtz-berlin.de

[d]IEK5-Photovoltaik, Forschungszentrum Jülich, Jülich, 52425, Germany

[e]Helmholtz-Zentrum Berlin für Materialien und Energie GmbH, Hahn-Meitner-Platz 1, Berlin, 14109, Germany

[f]Faculty of Engineering and CENIDE, University of Duisburg-Essen, Carl-Benz-Str. 199, Duisburg, 47057, Germany

† Electronic supplementary information (ESI) available. See DOI: https://doi.org/10.1039/d4se01321b

‡ Authors contributed equally.

efficient devices. Due to the size difference between Cl^- and I^-, the Cl^- ion is pushed to the surface of the perovskite crystallites during crystallisation also causing a Sn-rich environment, while favourably changing the energy level alignment and improving charge collection[17] by directing the growth of larger grains for better film coverage.[18] Despite the advances in controlling crystallisation, the reports on printed Sn perovskites has been scare.[19,20] This is unlike Pb perovskite solar cells which have been printed with PCE reaching over 20%.[21–25]

LaMer theory is the most used model to describe the nucleation and growth of crystalline materials from solution.[26] According to this theory, after coating, the wet perovskite film undergoes four phases, as depicted in Fig. 1a. Initially, the solute concentration is lower than the saturation limit and the solution is in its stable phase. Over time, an increasing amount of solvent is removed from the thin film by evaporation or extraction, and the concentration of the solution overcomes the saturation threshold. In this metastable phase, the solutes can thermodynamically form nuclei, but the film remains liquid, as it is kinetically stable. If the concentration of the solution is allowed to increase further, the thin film undergoes spontaneous burst nucleation. As the number of nuclei increases the

concentration of the thin film decreases leading to the fourth phase of crystal growth. This general picture can be slightly modified to consider the kinetics of the process. If the rate of solvent evaporation increases during the first two phases, the slope of the curve increases, as shown in Fig. 1b. This can be achieved by changing external process parameters, such as higher substrate temperature or higher convective flux (*i.e.*, spin coater rotation speed), or as mentioned above by solvent or additive engineering. Although the slope and shape of the curve change, the saturation threshold remains unaffected, as it is a thermodynamic parameter of the system; however, the minimum concentration for spontaneous nucleation increases.[27] The effect of this change is two-fold: the number of nuclei formed is higher due to higher supersaturation; the decrease in the solution concentration is faster because of the larger number of crystallization centers. The overall effect on perovskite crystallization is that a faster evaporation rate leads to a larger number of small grains, which is considered a sub-optimal morphology for perovskite solar cells due to high grain borders and, therefore, defects. However, a slow rate of solvent evaporation leads to a small number of nuclei, which grow slowly and form undesirable isolated dendrite structures.[28]

In this work, we introduce a new antisolvent-free approach for Sn perovskite film crystallization that utilizes a short gas pulse as a nucleation trigger and new additives that optimize the metastable and nucleation burst rates, leading to high-quality perovskite film formation. This enabled us to fabricate the first Sn perovskite films printed successfully *via* an industrially scalable slot-die coating technique. High-quality films were printed on 25 mm × 75 mm and 50 × 50 mm substrates. *In situ* photoluminescence (PL) and transmission spectroscopy were used to probe the crystallization dynamics and enabled us to compare the additives and conditions to achieve compact and pinhole-free films *via* slot-die coating. The champion printed device has 5.38% PCE for 0.1 cm² active area and 4.02% for 1 cm² active area and uses the new perovskite additive $MASnCl_3$. This is the first report of a slot die-coated Sn-perovskite solar cell, demonstrating that despite its ultrafast crystallization kinetics roll-to-roll production using this technology is entirely possible. To further explore its potential technological applications at scale, we also demonstrate the feasibility of using Sn-perovskite solar cells for indoor photovoltaics.
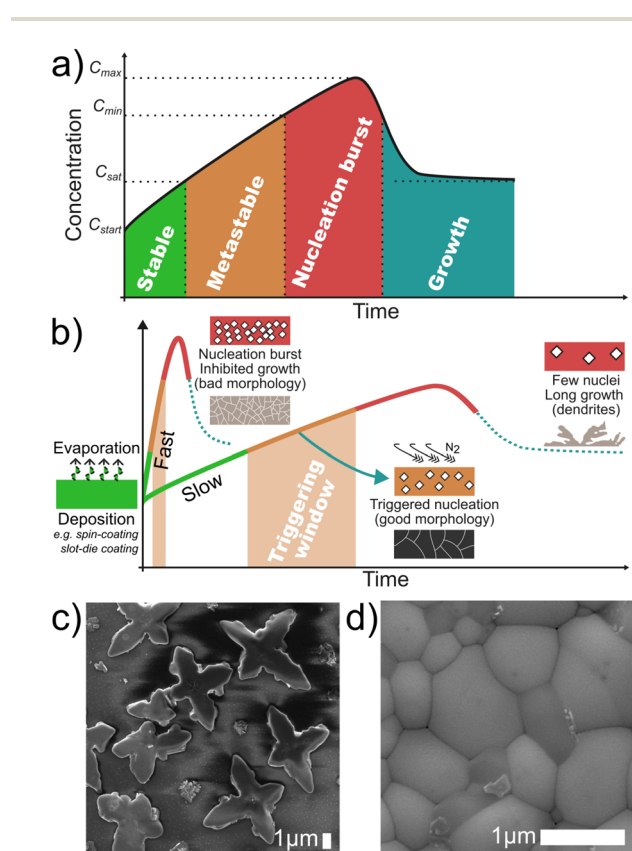

Fig. 1 (a) Representation of La Mer theory of crystallization (precursor concentration *vs.* time) showing the four fundamental phases of crystallization: stable, metastable, nucleation burst, and growth; (b) pictorial representation of the grain morphology of perovskite films formed *via* three different crystallization modes: fast solvent evaporation, slow solvent evaporation, and triggered crystallization. SEM micrography of grain morphologies; (c) without and (d) with crystallization triggering investigated in this study.

Slot-die coated films, optimising crystallization *via in situ* optical analysis

In the crystallization mechanism shown in Fig. 1a, the nucleation-growth process can be controlled using a triggering action during the metastable phase of the thin liquid film.[29] For Pb-perovskites, the most common trigger is the dripping of an antisolvent, whereas for single step Sn perovskite coating this has been the only option. Here we tested a trigger based on a short pulse of inert gas instead of antisolvent on slot-die coated films on 25 mm × 75 mm glass substrates. The precursor solution was made of FAI and SnI_2 dissolved in DMF :

*t*BP 6 : 4 volume ratio. *t*BP was used as a complexing agent to slow down the dynamic of crystallisation *via* formation of intermediate phases.[12] We observed that the brief blow of N_2 successfully triggers perovskite nucleation (Fig. 1b) to produce a morphology consisting of compact and large grains (Fig. 1d), instead of the dendritic structures seen without the gas pulse trigger (Fig. 1c). Printed films appeared red after the gas pulse but after annealing on a hot plate at 140 °C converted to black. In Pb perovskites, the timing of the nucleation trigger is known to be crucial for achieving dense and uniform films with well-oriented and large grains.[30] Here, too, the timing of the gas pulse had to be optimized, as otherwise films were found to eventually crystallize without the outside trigger and produce very poor morphologies unsuitable for device fabrication, as shown in Fig. S1.†

Additives were introduced to the precursor solution to change the slope of the crystallization curve (Fig. 1b). Initially three additives were tested (2.5 mol% concentration): $SnCl_2$, a popular additive for Sn perovskites;[13] MACl, a popular additive for $FAPbI_3$ systems because of its ability to induce intermediate phases;[31] and SnF_2. The Sn-perovskite films with the corresponding additives are denoted as FASI-SnCl$_2$, FASI-MACl, and FASI-SnF$_2$. It was observed from the *in situ* PL spectra in Fig. 2a that FASI-SnCl$_2$ and FASI-MACl had drastically different crystallization kinetics. Aiming at an intermediate crystallization rate, a new additive $MASnCl_3$ (2.5 mol% concentration) was then created by mixing equimolar amounts of MACl and SnCl$_2$. $MASnCl_3$ has been reported to have a perovskite structure.[32,33] A

solubility test was carried out for each additive by preparing 1M stock solutions in DMF, results shown in Fig. S2.† $SnCl_2$ dissolved in DMF, while MACl had a low solubility in either DMF or *t*BP. Since $MASnCl_3$ dissolved fine, we suggest that MACl binds with $SnCl_2$ to dissolve in the precursor solution by forming $MASnCl_3$.

With the trigger, uniform films were successfully printed. Without the air pulse trigger, the films with all additives eventually self-crystallized and produced poor morphologies that were unsuitable for device fabrication (Fig. S1†). The final PL peak energies of the samples (Fig. 2d and Table S1†) indicate the successful formation of high-quality FASnI$_3$ films,[34] except for FASI-MACl, which displayed a slightly higher bandgap PL, possibly owing to distorted structures or vacancies.

Immediately after the slot die coating, the wet film was placed onto the *in situ* setup (shown in Fig. S3†), and after a short gas pulse was applied, PL and transmission were recorded for 120 s (the natural drying time at room temperature under N_2 environment) with a 1 s interval time to probe the effect of the gas pulse on the crystallization kinetics. PL signals arise from emissive species formed in the film during crystallization, and the PL peak energy is a direct indicator of their bandgap, while a high PL intensity is linked to high-density and defect-free crystals.[35–39] Fig. 2a presents the PL spectra evolution for all four films before the final thermal annealing (140 °C on a hot plate). FASI-SnCl$_2$, FASI-MASnCl$_3$ and FASI-SnF$_2$ each showed a well-defined PL peak in the range of 1.7–1.8 eV formed immediately after the application of the gas pulse trigger. We link the formation of this peak to the burst nucleation of FASnI$_3$ perovskite nanocrystals triggered by the gas pulse, as depicted in Fig. 1a and b.[30,40] From the color maps in Fig. 2a, it is evident that FASI-SnF$_2$ exhibits the fastest nucleation and crystal growth, while FASI-MASnCl$_3$ has the slowest evolving PL and hence slowest crystallization. FASI-MACl did not exhibit PL evolution until the sample was moved to the hot plate (when crystallization occurred), indicating that the gas pulse did not trigger nucleation in this sample. The *in situ* transmission data (shown in Fig. S4†) is consistent with this observation and show only precursor absorption from FASI-MACl. Furthermore, both the PL intensity and energy of FASI-SnF$_2$ and FASI-SnCl$_2$ approach a plateau, as expected from the crystallization mechanism shown in Fig. 1, where the plateau occurs owing to a drop in solute supersaturation and termination of the nucleation process.[41] These *in situ* results reveal that additives can be used to control the crystallization rates of gas-triggered films. They also reveal that under the studied conditions, a Sn^{2+}-rich environment enables faster nucleation, consistent with previous studies of additives,[33] while MA^+ slows down this process likely due to the formation of a strong MA-SnI$_3$-*t*BP adduct in addition to the FA-SnI$_3$-*t*BP adducts.[12,42]

A closer look at the PL intensity and PL energy changes as a function of time in Fig. 2b–d reveals that there are two distinct nucleation events in FASI-SnCl$_2$ and FASI-SnF$_2$, and even in FASI-MASnCl$_3$. The first stage is complete within 3 seconds of the gas pulse and driven purely by fast solvent evaporation forced by the gas blow, while the second stage continues for tens of seconds and can be linked to the more gradual
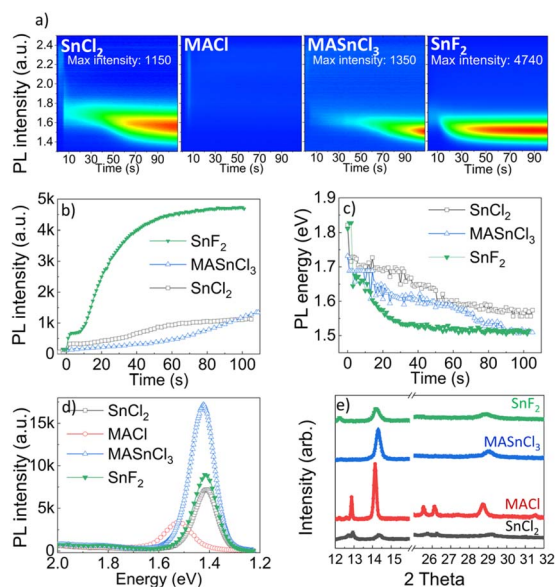

Fig. 2 (a) *In situ* PL measurements on slot-die coated films (contour plots with blue being the zero baseline and red being the maxima) printed with FASI-SnCl$_2$, FASI-MACl, FASI-MASnCl$_3$ and FASI-SnF$_2$. For a better comparison, the intensities of each measurement were normalized to the maximum PL intensity detected during the entire experiment. No signal evolution was observed for FASI-MACl. The corresponding *in situ* (b) PL peak intensity and (c) peak position changes as a function of time; FASI-MACl was excluded because of a lack of signal. The results after thermal annealing include the following: (d) steady-state PL spectra and (e) X-ray diffraction.

evaporation at room temperature of the more volatile of the two solvents, DMF. The existence of the two nucleation stages shows that the slot-die coated wet film is close to the metastable phase (Fig. 1) right before the gas pulse application (which forces evaporation and some nucleation likely on the top surface of the film). Despite the presence of stable nuclei after the gas pulse, as evidenced by the presence of PL, the second nucleation stage starts only after approximately 10 seconds when there is a transition from the metastable to the nucleation burst phase. The second stage was controlled by the additive, where the rate of crystallization followed the order: $SnF_2 >$ $SnCl_2 >$ $MASnCl_3 >$ MACl. The faster crystallisation for FASI-MASnCl$_3$ compared to FASI-MACl is likely due to MA$^+$ binding in the MASnCl$_3$ perovskite structure and minimising the effect from the MA-SnI$_3$-tBP adducts formation.[43] The final stage of crystallization occurs during thermal annealing when the leftover DMF and the higher-boiling-point tBP solvent are evaporated. FASI-SnCl$_2$, FASI-SnF$_2$ and FASI-MASnCl$_3$ end up with a PL peak maximum in between 1.41 and 1.42, indicative of high quality FASnI$_3$ films (Fig. 2d).[34,44] The small peak shift for FASI-MASnCl$_3$ could be due to Cl$^-$ and MA$^+$ incorporation in the FASnI$_3$ crystal structure forming mixed perovskite. However, FASI-MACl's PL peak is at 1.52 eV, which can be explained by the incorporation of Cl$^-$ in the crystal lattice.[3,44]

Structural characterization

X-ray diffraction (XRD) experiments were conducted to analyze the crystal structures of the four perovskite films (Fig. 2e and Table S2†). Note that the samples had to be exposed to air for a short time (<5 min) during sample loading, inevitably leading to oxidation. For FASnI$_3$ films with an orthorhombic ($Amm2$) crystal structure, two dominant peaks can be identified, which are located around 14.0° corresponding to the (100) crystal plane and 28.22° corresponding to the (200) crystal plane. All four films showed the above two peaks with some differences in full width at half maximum, intensity, and peak position, which originate from their different crystallization kinetics and compositions. For the FASI-SnCl$_2$ films, double peaks at 12.75° and 12.94° were assigned to the SnI$_4$ species,[45] indicating Sn oxidation. The FASI-MACl films showed sharp peaks corresponding to the (100) and (200) planes and strong SnI$_4$ peaks at 12.87° and 25.53°. The other two peaks at 26.13° could not be identified, while the low-intensity peak at 31.55° corresponded to the (122) plane of FASnI$_3$,[46] suggesting more disordered films for this sample. The XRD pattern of FASI-MASnCl$_3$ has only two peaks corresponding to the (100) and (200) planes, indicating preferential perovskite crystallization with a better stability compared to FASI-SnCl$_2$ and FASI-MACl. The small shift in diffraction peaks for FASI-MASnCl$_3$ (similar to FASI-SnCl$_2$) could be due to Cl$^-$ incorporation in the crystal structure. For FASI-SnF$_2$, the two main peaks showed lower intensities than for FASI-MASnCl$_3$, with one extra peak at approximately 12.24°. The peak positions and the corresponding species are listed in Table S2.† Similarly to XRD, SEM images (Fig. S5† on glass and Fig. S6† on PEDOT/ITO) indicated the presence of either point defects, undesirable particles, or poor grain boundaries on the

surface of most samples, except for the best quality films of FASI-MASnCl$_3$ and FASI-SnF$_2$ deposited on PEDOT : PSS. From these data, it can be concluded that all samples produced predominantly FASnI$_3$ with preferential crystallization with (100) planes parallel to the film surface.[46] FASI-MASnCl$_3$ had the cleanest diffraction pattern and surface quality without contaminants or defects, suggesting the highest quality of crystals and densely packed films for this sample,[47,48] which agrees with the PL spectral intensities of the annealed films. It also highlights the importance of controlling the rate of crystallisation that neither too fast nor too slow nucleation is beneficial for growing high quality perovskite crystals for slot-die coated films.

Fabrication of slot-die coated devices

FASnI$_3$ devices were fabricated by slot-die coating the Sn-perovskite films with the architecture: glass/ITO/PEDOT : PSS/ FASnI$_3$/C$_{60}$/BCP/Ag. Fig. 3 presents the JV curves of the champion devices and the distribution of device parameters. FASI-MASnCl$_3$ and FASI-SnF$_2$ showed the best J_{sc}, corresponding well to their higher steady-state PL and compact grains, as shown in Fig. S6† in SEM. FASI-MACl showed a lower J_{sc}, which is partly due to the lower IPCE from 550 to 850 nm (Fig. S7†). From IPCE, the bandgap of all devices could be determined as roughly 1.41 eV (Fig. S7†), this is consistent with the bandgap derived from PL for SnCl$_2$, MASnCl$_3$ and SnF$_2$. However, for FASI-MACl the bandgap derived from PL was 1.52 eV. This suggests an anti-Stokes shift of more than 100 meV. The spectral shape shift of the IPCE in FASI-MACl and to an extent in FASI-SnCl$_2$ suggests that different photoactive species are formed. One possible
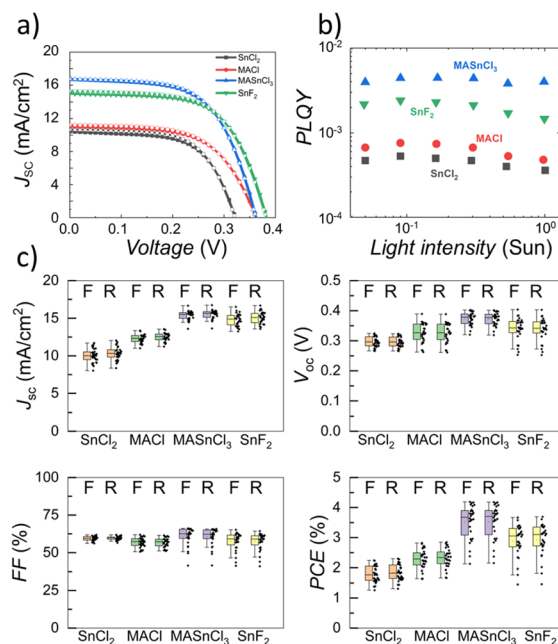

Fig. 3 Comparison of the performance of FASnI$_3$ devices printed with the four additives studied, SnCl$_2$, MACl, MASnCl$_3$, SnF$_2$. (a) JV scans; (b) light–intensity–dependent photoluminescence quantum yield of each sample (full device stack); (c) JV performance distribution (F for forward and R for reverse scans) of each sample.

explanation is that some $MA/FASnCl_3$ was formed at the expense of $FASnI_3$ or greater density of Sn vacancies are present in the films.[34,44] V_{oc} followed the same trend as J_{sc}, while the fill factor remained similar between samples. From the JV data in Fig. 3, it appears that the best additive is $MASnCl_3$ and the FASI-$MASnCl_3$ device reaches $\eta = 4.2\%$.

To investigate recombination in the full device stacks, we measured the photoluminescence quantum yield (PLQY). The full spectra of the light-intensity-dependent steady-state photoluminescence are shown in Fig. S8.† From Fig. 3b, it can be seen that the PLQY of each sample is independent of light intensity, which can be explained by the high doping density of Sn perovskites.[49,50] For a doped semiconductor in low-level injection, all recombination mechanisms become linear in charge carrier concentration, so that the PLQY remains constant.[51] Furthermore, the PLQY values are high in comparison to what is expected from the measured V_{oc} values. This indicates an energetic mismatch in the device.[52–54] In reverse, it follows that the quality of the printed Sn perovskites is higher than the low V_{oc} values suggest. Comparing between additives, FASI-$MASnCl_3$ shows the highest PLQY which is consistent with its better performance in devices and better film and crystal quality. Furthermore, the bulk is not primarily responsible for the V_{oc} loss, which could be reduced by using an ETL with energy levels that better match the perovskite layer.[55] Indeed, the PLQY is comparable to some high-performance Pb perovskite solar cells.[56]

The $MASnCl_3$ molar concentration was optimized to further improve the performance. The results (Fig. S9†) show that 7.5 mol% is the optimal molar concentration. We suggest that up to 7.5 mol%, $MASnCl_3$ can be incorporated into the $FASnI_3$ structure and form a mixed perovskite phase, which causes the small PL peak shift and broadening. It appears that a phase separation occurs between 7.5 mol% and 10 mol%, where due to energy level misalignment, the $MASnCl_3$ phase starts to form a blocking layer and at 12.5 mol%, it becomes a blocking layer causing decreased shunt resistance hindering the extraction of charge carriers. Simultaneously, the series resistance, derived from the slope dV/dJ at V_{oc}, increased as the additive concentration increased from 7.5 to 10 mol%. If a new phase with a larger bandgap is formed, then the increase in J_{sc} with $MASnCl_3$ is impressive, as it means that the mixed phase also has a better charge carrier extraction capability. For 7.5 mol% $MASnCl_3$ added devices, the best pixel had $J_{sc} = 16.64$ mA cm^{-2}, $V_{oc} = 0.49$ V, and FF = 65.85%. The device efficiency was $\eta = 5.38\%$ for an area of 0.1 cm^2.

To demonstrate the potential for large-area devices, 50 mm × 50 mm substrates were used to make another batch using optimized parameters from the results shown above. We first performed photoluminescence imaging (PLI) on the ITO/PEDOT : PSS/$FASnI_3$ films. The results are shown in Fig. S10.† The uniform PL intensity distribution suggests a uniform $FASnI_3$ film was formed from the slot-die coating on the large substrate. A batch of devices was subsequently fabricated with a 1 cm^2 and 5 cm^2 device area. For the champion pixels, 1 cm^2 pixel demonstrated values of $J_{sc} = 20.1$ mA cm^{-2}, $V_{oc} = 0.42$ V, FF = 45.7% and $\eta = 4.02\%$, while a 5 cm^2 pixel demonstrated $J_{sc} = 15.83$ mA cm^{-2}, $V_{oc} = 0.44$ V, FF = 32.68%, and $\eta = 2.31\%$. The low FF was attributed to the lack of an optimised testing setup, as two crocodile clips were used to make contact, leading to poor charge extraction during the measurement. Nevertheless, both PLI and solar cell performances demonstrated the potential and reproducibility for large-area $FASnI_3$ deposition with the slot die coating technique, especially considering that the large-area devices were fabricated at a different laboratory with different equipment compared to the smaller 0.1 cm^2 slot die coated devices.

Slot-die coated Sn-perovskite PV for indoor applications

One possible application for printed Sn perovskites is indoor PV, where its potentially lower toxicity compared to Pb perovskites can be beneficial. We tested the FASI-$MASnCl_3$ devices with different $MASnCl_3$ concentrations using LED light to simulate indoor conditions. As shown in Fig. 4, FASI-7.5 mol% $MASnCl_3$ exhibited the best performance across a range of light intensities. At 0.03 sun, it obtained $\eta = 5.4\%$. Fig. S11† presents the V_{oc} changes at the LED intensities studied. The combination of a lead-free device and deposition via slot die coating is a promising breakthrough for indoor PV applications.
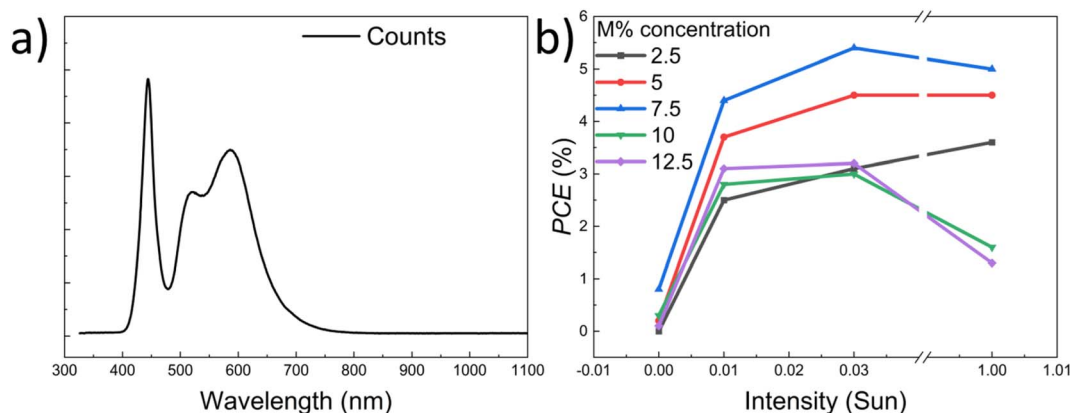

Fig. 4   (a) Spectrum of the LED used to test indoor PV performance and (b) the corresponding PCE under different light intensities for FASI with different mol% concentration of $MASnCl_3$.

Conclusion

Sn perovskite solar cell efficiencies have increased significantly recently and are now reaching 14%. However, roll-to-roll printing of $FASnI_3$ solar cells has not yet been achieved. Here, we address the key challenge of uncontrolled crystallization in this material to successfully print Sn-perovskite solar cells via slot-die coating. A novel crystallization approach was applied with a combination of solvent and additive engineering and a gas pulse trigger for Sn perovskite nucleation in the slot-die-coated wet films. $FASnI_3$ films were coated on different area substrates using a DMF : tBP solvent mixture, avoiding the use of oxidative DMSO while slowing down crystallisation via a tBP-based intermediate phase. The rate of crystallization was controlled using the additives $SnCl_2$, SnF_2, MACl, and $MASnCl_3$. In situ PL and transmission measurements performed during and after gas pulsing showed that finding an optimal kinetics of nucleation is extremely beneficial for producing high quality solar cell devices. The best perovskite films were fabricated with $MASnCl_3$ as an additive, showing intermediate crystallisation kinetics amongst the studied systems, leading to a pinhole-free morphology, highest PLQY. This result is consistent with the need to create a Sn-rich environment to compensate for Sn vacancy defects and minimize Sn^{2+} oxidation during crystallisation, and the usefulness of Cl^- to favourably direct crystal growth and in improving charge collection, and the role of MA^+ in slowing down crystallisation through intermediate adduct formation. Optimisation of the FASI-$MASnCl_3$ composition led to the fabrication of devices achieving $\eta = 5.38\%$ for 0.1 cm^2 and $\eta = 4.02\%$ for 1 cm^2 and $\eta = 2.31\%$ for 5 cm^2 device area. The device was also tested under indoor light conditions and demonstrated a similarly high performance. Therefore, we report the first lead-free Sn perovskite solar cells achieved via an antisolvent-free and entirely scalable method that is suitable for roll-to-roll production, demonstrating the potential of this technology for future PV applications.

Methods section

Materials

Unless otherwise specified, the chemicals were used as received without further purification. Tin(II) iodide (SnI_2), ethylenediammonium diiodide (EDAI$_2$, >98%), N,N-dimethylformamide (anhydrous, 99.8%), 4-(tert-butyl) pyridine (98%), bathocuproine (BCP), and silver beads were purchased from Sigma-Aldrich and used as received. Formamidinium iodide (FAI, >98%) was purchased from Dyenamo. Patterned ITO glass slides were purchased from Ossila. PEDOT : PSS polymer dispersion in both water and toluene (CLEVIOS™) was purchased from Heraeus.

Perovskite solution preparation

A solution of SnI_2 was dissolved in pure DMF first. The solution was kept under shaking at ambient temperature for one hour to dissolve the tin salts completely. FAI powder was scaled in a new vial, and the proper amount of the SnI_2 solution was added to the powder, leading to a desired FA : Sn molar ratio. The solution was kept under shaking for an hour at ambient temperature for the complete dissolution of FAI. Afterwards, tBP was added to achieve the desired volume ratio between DMF and tBP (6 : 4 for slot die coating). EDAI$_2$, $SnCl_2$ and $MASnCl_3$ were dissolved in separate vials with pure DMF to make a 1M stock solution. MACl and SnF_2 were added as powers due to poor solubility in DMF. Finally, the $FASnI_3$ solution (0.6 M for slot die coating) with different additives was achieved by adding the corresponding additives and further shaking for one hour. All additives were 2.5 mol% in the final solutions. For the investigation of $MASnCl_3$ concentration, five solutions were prepared: 2.5 mol%, 5 mol%, 7.5 mol%, 10 mol% and 12.5 mol%. The solution was filtered with a 0.2 μm PTFE filter before use.

Solar cells fabrication

An inverted structure was chosen for the PSCs fabricated with the following stacking: glass/ITO/PEDOT : PSS/$FASnI_3$/C_{60}/BCP/Ag. Patterned indium tin oxide (ITO) coated glasses were first washed in an ultrasonic thermal bath at 40 °C with the following procedure: 15 minutes with a liquid detergent dissolved in deionised water (2% V/V); rinsed in deionised water and sonicated for 5 minutes; rinsed in acetone and then sonicated for 15 minutes; rinsed in ethanol and then sonicated for 15.

For slot die coating, clean substrates were treated using UV ozone cleaner (Ossila) and aqueous PEDOT was deposited in ambient conditions. The deposition remained the same. Films were annealed at 120 °C for 20 min. After moving the substrates into the glovebox, substrates were placed on a slot die coater (Ossila) for perovskite deposition. The stage was kept at 40 °C during the coating. The moving speed was set at 5 mm s^{-1}; the dispense rate was set at 1 μL s^{-1}. After the coating, the substrate was removed from the stage, and a handheld air blow gun was used to blow the surface at a distance of 10 cm quickly. Ideally, an automated air knife could be fitted inline so the gas pulse happens during the coating. This could not be achieved because the stage has no vacuum suction function to fixate the substrate or enough coating distance (maximum 10 cm) to fit the air knife. After the quick blow, the film turned red and was immediately placed onto a hot plate for annealing at 140 °C for 20 min.

The gas blow was applied with a 5 bar N_2 gas gun in the glovebox from a 10 cm distance above for all perovskite deposition experiments.

The ETL and the silver electrode were deposited using a thermal evaporation chamber at a high vacuum (<10^{-6} bar). The thickness of the three layers, C_{60}, BCP and Ag, were 75, 7 and 150 nm, respectively.

For slot die coating of large area (50 × 50 mm) devices, the process was repeated at a different lab with same deposition parameters. All equipment remained the same except the slot die coating was performed on the larger FOM alphaSC slot die coater and a Keithley 2400 was used for measurement with a WAVELABS Sinus LED solar simulator.

In situ PL and transmission measurement

The in situ PL and transmission measurement was conducted in a N_2-filled glovebox. The excitation was provided by Avantes

portable LED laser (AvaLight-HPLED, 3.4 mW, 405 nm). A Wasatch f/2 high throughput spectrometer (WP-VISNIR-R-S-50) captured the PL response. Thorlabs Reflection probe RP23 was used for the measurement at reflection mode. For transmission, Avantes AvaLight-DHc was used as light source, Avantes AvaSpec-ULS2048CL-EVO was used as the spectrometer, SMA-905 optic fibres and M6 tapped optical breadboards were purchased from Thorlabs. The set-up is illustrated in Fig. S3.†

PLQY measurement

The photoluminescence quantum yield was measured with a calibrated Quantum Yield Berlin LuQY Pro setup. The samples were illuminated in an integrating sphere with a 532 nm laser with intensities between 0.05 and 1 sun equivalence. For each illumination intensity, five spectra were recorded and averaged.

Photovoltaic characterisation

The multimodal Arkeo machine from Cicci Research s.r.l. was used to characterise the solar cell performance in the glovebox. The device's current density–voltage (J–V) characteristics were tested using a 12 LED solar simulator with a calibrated optical power density of 100 mW cm^{-2}. PSC J–V characteristics were measured every 10 mV with a sample rate of 100 mV s^{-1}. Incident photon to current conversion efficiency (IPCE) were measured using a commercial apparatus (Arkeo-Ariadne, Cicci Research s.r.l.) based on a 300 Watt Xenon lamp. The monochromatic light intensity was calibrated using a Hamamatsu S1337 Si-calibrated photodiode.

Structural characterisation

Scanning electron microscopy (FEI inspect F) was used for observing perovskite morphology and device architecture. X-ray diffraction was performed using a Siemens D5005 diffractometer from 5° to 70° using Cu K$_\alpha$ radiation. Crystal peaks were identified using the International Centre for Diffraction Data (ICDD) database.

Photoluminescence imaging (PLI)

PL imaging was done with a camera using a silicon CCD detector. As excitation source an array of 520 nm LEDs were used to provide homogeneous illumination over the whole imaged area. The integration time was optimized for each sample to make maximal use of the 16 bit dynamic range of the CCD detector. Additionally, a 700 nm long pass and an 850 nm short pass filter were used between sample and camera.

Data availability

All data from the manuscript, scalable slot-die printing of lead-free tin perovskite solar cells *via* controlled crystallization, is freely available upon request from the authors.

Conflicts of interest

The authors declare no conflict of interest.

References

1 A. Abate, Perovskite solar cells go lead free, *Joule*, 2017, **1**, 659–664.
2 N. K. Noel, *et al.*, Lead-free organic–inorganic tin halide perovskites for photovoltaic applications, *Energy Environ. Sci.*, 2014, **7**, 3061–3068.
3 F. Hao, C. C. Stoumpos, D. H. Cao, R. P. H. Chang and M. G. Kanatzidis, Lead-free solid-state organic–inorganic halide perovskite solar cells, *Nat. Photonics*, 2014, **8**, 489–494.
4 J. Chen, *et al.*, Spatially isomeric fulleropyrrolidines enable controlled stacking of perovskite colloids for high-performance tin-based perovskite solar cells, *Angew. Chem., Int. Ed.*, 2025, e202420150.
5 M. De Bastiani, *et al.*, Monolithic perovskite/silicon tandems with >28% efficiency: role of silicon-surface texture on perovskite properties, *Adv. Funct. Mater.*, 2023, **33**, 2205557.
6 *Best Research-Cell Efficiency Chart | Photovoltaic Research*, NREL, https://www.nrel.gov/pv/cell-efficiency.html.
7 J. Wang, *et al.*, Controlling the crystallization kinetics of lead-free tin halide perovskites for high performance green photovoltaics, *Adv. Energy Mater.*, 2021, **11**, 2102131.
8 T. Wu, *et al.*, Lead-free tin perovskite solar cells, *Joule*, 2021, **5**, 863–886.
9 H. Dong, *et al.*, Crystallization dynamics of sn-based perovskite thin films: toward efficient and stable photovoltaic devices, *Adv. Energy Mater.*, 2022, **12**, 1–28.
10 F. Li, *et al.*, A cation-exchange approach for the fabrication of efficient methylammonium tin iodide perovskite solar cells, *Angew. Chem., Int. Ed.*, 2019, **58**, 6688–6692.
11 P. Wang, *et al.*, Ion exchange/insertion reactions for fabrication of efficient methylammonium tin iodide perovskite solar cells, *Adv. Sci.*, 2020, **7**, 1903047.
12 G. Nasti, *et al.*, Pyridine controlled tin perovskite crystallization, *ACS Energy Lett.*, 2022, **7**, 3197–3203.
13 K. P. Marshall, M. Walker, R. I. Walton and R. A. Hatton, Enhanced stability and efficiency in hole-transport-layer-free CsSnI3 perovskite photovoltaics, *Nat. Energy*, 2016, **1**, 1–9.
14 S. Gupta, D. Cahen and G. Hodes, How SnF2 impacts the material properties of lead-free tin perovskites, *J. Phys. Chem. C*, 2018, **122**, 13926–13936.
15 S. J. Lee, *et al.*, Fabrication of efficient formamidinium tin iodide perovskite solar cells through SnF2-pyrazine complex, *J. Am. Chem. Soc.*, 2016, **138**, 3974–3977.
16 M. Xiao, *et al.*, Tin-based perovskite with improved coverage and crystallinity through tin-fluoride-assisted heterogeneous nucleation, *Adv. Opt. Mater.*, 2018, **6**, 1700615.

17 B. B. Yu, *et al.*, Synergy effect of both 2,2,2-trifluoroethylamine hydrochloride and SnF2 for highly stable FASnI$_{3-x}$Cl$_x$ perovskite solar cells, *Sol. RRL*, 2019, **3**, 1800290.

18 M. E. Kayesh, *et al.*, Enhanced photovoltaic performance of FASnI3-based perovskite solar cells with hydrazinium chloride coadditive, *ACS Energy Lett.*, 2018, **3**, 1584–1589.

19 L. He, *et al.*, Efficient anti-solvent-free spin-coated and printed sn-perovskite solar cells with crystal-based precursor solutions, *Matter*, 2020, **2**, 167–180.

20 W. Żuraw, *et al.*, Large-area, flexible, lead-free sn-perovskite solar modules, *ACS Energy Lett.*, 2023, **8**, 4885–4887.

21 F. Xu, *et al.*, Potassium thiocyanate-assisted enhancement of slot-die-coated perovskite films for high-performance solar cells, *Small Sci.*, 2021, **1**, 2000044.

22 J. Li, *et al.*, 20.8% slot-die coated MAPbI3 perovskite solar cells by optimal DMSO-content and age of 2-ME based precursor inks, *Adv. Energy Mater.*, 2021, **11**, 2003460.

23 A. S. Subbiah, *et al.*, High-performance perovskite single-junction and textured perovskite/silicon tandem solar cells *via* slot-die-coating, *ACS Energy Lett.*, 2020, **5**, 3034–3040.

24 M. Du, *et al.*, High-pressure nitrogen-extraction and effective passivation to attain highest large-area perovskite solar module efficiency, *Adv. Mater.*, 2020, **32**, 2004979.

25 T. Bu, *et al.*, Lead halide-templated crystallization of methylamine-free perovskite for efficient photovoltaic modules, *Science*, 2021, **372**, 1327–1332.

26 C. B. Whitehead, S. Özkar and R. G. Finke, LaMer's 1950 model of particle formation: a review and critical analysis of its classical nucleation and fluctuation theory basis, of competing models and mechanisms for phase-changes and particle formation, and then of its application to silver halide, semiconductor, metal, and metal-oxide nanoparticles, *Mater. Adv.*, 2021, **2**, 186–235.

27 S. Kolahgar-Azari, *et al.*, Semicrystalline polymer micro/nanostructures formed by droplet evaporation of aqueous poly(ethylene oxide) solutions: effect of solution concentration, *Langmuir*, 2022, **38**, 15063–15076.

28 A. R. Pascoe, *et al.*, Directing nucleation and growth kinetics in solution-processed hybrid perovskite thin-films, *Sci. China Mater.*, 2017, **60**, 617–628.

29 D.-K. Lee, K.-S. Lim, J.-W. Lee and N.-G. Park, Scalable perovskite coating *via* anti-solvent-free Lewis acid–base adduct engineering for efficient perovskite solar modules, *J. Mater. Chem. A*, 2021, **9**, 3018–3028.

30 T.-B. Song, *et al.*, Dynamics of antisolvent processed hybrid metal halide perovskites studied by *in situ* photoluminescence and its influence on optoelectronic properties, *ACS Appl. Energy Mater.*, 2020, **3**, 2386–2393.

31 M. Kim, *et al.*, Methylammonium chloride induces intermediate phase stabilization for efficient perovskite solar cells, *Joule*, 2019, **3**, 2179–2192.

32 D. J. Kubicki, *et al.*, Local structure and dynamics in methylammonium, formamidinium, and cesium tin(II) mixed-halide perovskites from 119Sn solid-state NMR, *J. Am. Chem. Soc.*, 2020, **142**, 7813–7826.

33 C. M. Tsai, *et al.*, Formation of stable tin perovskites co-crystallized with three halides for carbon-based mesoscopic lead-free perovskite solar cells, *Angew. Chem., Int. Ed.*, 2017, **56**, 13819–13823.

34 M. Ozaki, *et al.*, Solvent-coordinated tin halide complexes as purified precursors for tin-based perovskites, *ACS Omega*, 2017, **2**, 7016–7021.

35 T. Huang, *et al.*, Performance-limiting formation dynamics in mixed-halide perovskites, *Sci. Adv.*, 2021, **7**, 1799.

36 F. Wang, *et al.*, 2D-quasi-2D-3D hierarchy structure for tin perovskite solar cells with enhanced efficiency and stability, *Joule*, 2018, **2**, 2732–2743.

37 T.-B. Song, *et al.*, Dynamics of antisolvent processed hybrid metal halide perovskites studied by *in situ* photoluminescence and its influence on optoelectronic properties, *ACS Appl. Energy Mater.*, 2020, **3**, 2386–2393.

38 T. Moot, *et al.*, CsI-antisolvent adduct formation in all-inorganic metal halide perovskites, *Adv. Energy Mater.*, 2020, **10**, 1–9.

39 T.-B. Song, *et al.*, Revealing the dynamics of hybrid metal halide perovskite formation *via* multimodal *in situ* probes, *Adv. Funct. Mater.*, 2020, **30**, 1908337.

40 V. K. LaMer and R. H. Dinegar, Theory, production and mechanism of formation of monodispersed hydrosols, *J. Am. Chem. Soc.*, 1950, **72**, 4847–4854.

41 P. G. Vekilov, The two-step mechanism of nucleation of crystals in solution, *Nanoscale*, 2010, **2**, 2346–2357.

42 C. Liu, Y. B. Cheng and Z. Ge, Understanding of perovskite crystal growth and film formation in scalable deposition processes, *Chem. Soc. Rev.*, 2020, **49**, 1653–1687.

43 C. Liu, Y. B. Cheng and Z. Ge, Understanding of perovskite crystal growth and film formation in scalable deposition processes, *Chem. Soc. Rev.*, 2020, **49**, 1653–1687.

44 R. L. Milot, *et al.*, The effects of doping density and temperature on the optoelectronic properties of formamidinium tin triiodide thin films, *Adv. Mater.*, 2018, **30**, 1804506.

45 E. Jokar, *et al.*, Slow surface passivation and crystal relaxation with additives to improve device performance and durability for tin-based perovskite solar cells, *Energy Environ. Sci.*, 2018, **11**, 2353–2362.

46 S. Shao, *et al.*, Highly reproducible sn-based hybrid perovskite solar cells with 9% efficiency, *Adv. Energy Mater.*, 2018, **8**, 1702019.

47 Z. Chen, *et al.*, Thin single crystal perovskite solar cells to harvest below-bandgap light absorption, *Nat. Commun.*, 2017, **8**, 1890.

48 Y. Lei, *et al.*, A fabrication process for flexible single-crystal perovskite devices, *Nature*, 2020, **583**, 790–795.

49 Y. Takahashi, H. Hasegawa, Y. Takahashi and T. Inabe, Hall mobility in tin iodide perovskite CH$_3$NH$_3$SnI$_3$: evidence for a doped semiconductor, *J. Solid State Chem.*, 2013, **205**, 39–43.

50 D. B. Mitzi, C. A. Feild, Z. Schlesinger and R. B. Laibowitz, Transport, optical, and magnetic properties of the conducting halide perovskite CH$_3$NH$_3$SnI$_3$, *J. Solid State Chem.*, 1995, **114**, 159–163.

51 M. Stolterfoht, *et al.*, The impact of energy alignment and interfacial recombination on the internal and external open-circuit voltage of perovskite solar cells, *Energy Environ. Sci.*, 2019, **12**, 2778–2788.

52 C. M. Wolff, *et al.*, Nonradiative recombination in perovskite solar cells: the role of interfaces, *Adv. Mater.*, 2019, **31**, 1902762.

53 P. Caprioglio, *et al.*, On the relation between the open-circuit voltage and quasi-fermi level splitting in efficient perovskite solar cells, *Adv. Energy Mater.*, 2019, **9**, 1901631.

54 J. Warby, *et al.*, Mismatch of quasi–fermi level splitting and V_{oc} in perovskite solar cells, *Adv. Energy Mater.*, 2023, **13**, 2303135.

55 W. Liu, *et al.*, Tin halide perovskite solar cells with open-circuit voltages approaching the shockley-queisser limit, *ACS Appl. Mater. Interfaces*, 2023, **15**, 32487–32495.

56 J. Warby, *et al.*, Understanding performance limiting interfacial recombination in pin perovskite solar cells, *Adv. Energy Mater.*, 2022, **12**, 2103567.